Nanocast nitrogen-containing ordered mesoporous carbons from glucosamine for selective CO_2 capture

E. Maruccia [a, b, c, **], M.A.O. Lourenço [a, 1], T. Priamushko [d], M. Bartoli [a], S. Bocchini [a], F.C. Pirri [a, e], G. Saracco [b, e], F. Kleitz [d], C. Gerbaldi [b, c, *]

[a] Center for Sustainable Future Technologies (CSFT), Istituto Italiano di Tecnologia (IIT), Via Livorno, 60, 10144, Torino, Italy
[b] GAME Lab, Department of Applied Science and Technology, Politecnico di Torino, Corso Duca Degli Abruzzi, 24, 10129, Torino, Italy
[c] National Reference Center for Electrochemical Energy Storage (GISEL) - INSTM, Via G. Giusti 9, Firenze, 50121, Italy
[d] Department of Inorganic Chemistry — Functional Materials, Faculty of Chemistry, University of Vienna, Währinger Strasse 42, 1090, Vienna, Austria
[e] Department of Applied Science and Technology, Politecnico di Torino, Corso Duca Degli Abruzzi, 24, 10129, Torino, Italy

ABSTRACT

D-glucosamine is investigated as a non-toxic and sustainable carbon/nitrogen (C/N) source for the templated synthesis of nitrogen-containing CMK-8 ordered mesoporous carbons (NOMCs) conceived for selective CO_2 uptake. Pyrolysis temperature is varied during nanocasting using the KIT-6 silica hard template to tailor microporosity and nitrogen inclusions. NOMCs exhibit large surface area ($600-1000$ m^2 g^{-1}) and excellent pore ordering. The CO_2/adsorbent interaction energy is estimated by the isosteric enthalpy of adsorption (~33–40 kJ mol^{-1}) and Henry's constants. The role of nitrogen content (~7 -12 at.%) and of each type of N-species on CO_2 adsorption is studied by X-ray photoelectron spectroscopy, and CO_2/N_2 selectivity is attributed, being pyridinic functionalities the most effective ones. NOMCs are tested at different temperatures, gas flow compositions, reversibility, and so on; in all tested conditions, they outperform a homologous bare sucrose-derived carbon. Enhancing micropore volume allows achieving maximum adsorption capacity in pure CO_2 (1.47 mmol g^{-1} at 30 °C/0.9 bar), whereas increasing surface N-content accounts for the highest selectivity in CO_2/N_2 mixtures (20/80 v/v) at 35 °C/1 bar (maximum CO_2 uptake 0.82 mmol g^{-1}). The combination of a suitable C/N precursor and the hard templating synthetic route is effective for obtaining high-performing, sustainable, and reusable selective CO_2 sorbents, without any activation steps or N-doping post-treatments.

© 2021 The Author(s). Published by Elsevier Ltd. This is an open access article under the CC BY-NC-ND license (http://creativecommons.org/licenses/by-nc-nd/4.0/).

1. Introduction

Nowadays, global warming is one of the most challenging issues. In 2020, the global average temperature exceeded approximately 1.2 °C of the preindustrial level [1], which is attributed to the incessant increase of anthropogenic greenhouse gases emissions. Among these, carbon dioxide (CO_2) gas is considered the biggest responsible for greenhouse effect [2]. Hence, a lot of efforts have been made in developing technologies with a low carbon footprint. As long as renewable resources become competitive to fully meet the energy demand and replace fossil fuels, carbon capture and storage (CCS) technologies play a crucial role in mitigating the effects of CO_2 emissions in the near future [3]. CCS methods for CO_2 sequestration are mainly based on absorption (bulk process) [4–6], adsorption (surface process) [7], membrane [8] and cryogenics [9] technologies. Technologies based on absorption are currently the most mature and industrialized, by using liquid amines that chemically interact with the CO_2 molecules [10]. However, several limitations have still to be solved, such as severe corrosion of the equipment and high energy consumption for absorbent regeneration [11]. To overcome these issues, adsorption technology benefits lower operation costs and adsorbent reusability compared with the other technologies [7].

Solid-sorbent families such as zeolites [12], metal-organic frameworks [13], porous silicas [14], porous polymers [15], and porous carbons [16] are the most used to capture CO_2, mainly *via*

---

* Corresponding author.
** Corresponding author.
E-mail addresses: elisa.maruccia@polito.it (E. Maruccia), claudio.gerbaldi@polito.it (C. Gerbaldi).
[1] CICECO - Aveiro Institute of Materials, Department of Chemistry, University of Aveiro, Campus Universitário de Santiago, Aveiro, 3810-193, Portugal.

physical adsorption. Among them, porous carbons are advantageous because they can be obtained with large surface area, tunable porous structure, and surface properties. At the same time, they have good thermal and chemical stability and resistance to moisture [17]. Their cost-effectiveness is related to the production process; commercial and cheap highly porous carbons are also available and used commercially, for instance, the ones derived from low-cost biomass feedstock [18]. A critical aspect of physical adsorbents is the low selectivity for CO_2 in a mixture with other gases, as typically occurs in flue gases [19]. The design of the pore architecture and the adjustment of the surface properties are the most used strategies for promoting a selective adsorbate-adsorbent interaction. It is generally agreed that micropores (<2 nm) and, in particular, ultramicropores (<0.7 nm) are crucial for boosting both CO_2 adsorption and selectivity because of the higher adsorption potential in very small pores [20−22]. However, in the microporous network, the CO_2 diffusion is affected by slow kinetics and inaccessibility [23]. An ordered porous architecture composed by combining micropores and mesopores improves the CO_2 uptake [23]. For instance, Vorokhta et al. [24] and Garcia et al. [25] observed the beneficial effects of a mutual contribution of the micropore content and the ordered mesoporosity in the CO_2 adsorption capacity and kinetics, respectively. Indeed, despite templated synthetic routes increas the overall cost of the process, by involving expensive chemicals and multiple time-consuming reaction steps, ordered mesoporous carbons (OMCs) are still competitive from an application point of view. Indeed, the ordered porous network facilitates gas transport and makes the adsorption sites available to the adsorbate. Moreover, OMCs represent a relevant model system to study composition and porosity parameters of the adsorbents.

The heteroatom incorporation onto the carbon surface is a widely explored strategy for enhancing the interaction with CO_2 [26]. Specific functionalization with N-based moieties is widely used for increasing the basicity of the carbon framework, thus promoting the interaction with the acidic CO_2 molecule [27]. However, microporosity and nitrogen doping are frequently obtained via post-synthesis processes, such as physical or chemical activation [28,29] and treatments with ammonia and/or functionalization with amine groups [30,31], respectively. Additional stages in the adsorbents preparation procedure increase time/energy consumptions, which in turn increase the overall cost and impact over industrial up-scaling.

In this study, an original, alternative approach for the synthesis of nitrogen-containing ordered mesoporous carbons (namely, NOMCs) is proposed, which are readily obtained by applying the well-known nanocasting technique. Chitin is the second most abundant natural polysaccharide, one derivative obtained from its hydrolysis is D-glucosamine. To our knowledge, the derived D-glucosamine hydrochloride is here explored for the first time as a sustainable source to obtain in a single-step, by the nanocasting approach, N-loaded ordered CMK-8-type mesoporous carbons conceived for greenhouse gas adsorption/separation. The novel NOMC materials are prepared by impregnating D-glucosamine into the pores of the KIT-6 ordered mesoporous silica hard-templates followed by pyrolysis and silica removal steps. Different KIT-6 hard templates and pyrolysis conditions are applied to induce changes in the porosity and in the amount and type of nitrogen functionalities of the NOMC materials. Their effects on CO_2 adsorption and selectivity are thoroughly investigated by a comprehensive set of physicochemical techniques. Particular interest is devoted to the CO_2 adsorption performances: different testing conditions (temperature and gas composition), selectivity, and reusability are evaluated, so as to unravel the feasibility of the use of the synthetized materials as efficient and highly selective CO_2 adsorbents in a circular economy perspective.

2. Materials and methods

2.1. Chemicals

Poly(ethylene glycol)-block-poly(propylene glycol)-block-poly(ethylene glycol) ($EO_{20}PO_{70}EO_{20}$, P123, Mn~5800), tetraethyl orthosilicate (TEOS, 98%), sucrose ($C_{12}H_{22}O_{11}$, $\geq$ 99.0%, namely S in this work) were purchased from Sigma-Aldrich. Ethanol (C_2H_6O, EtOH, 96%) was purchased from Brenntag. 1-butanol (BuOH, 99%), sodium hydroxide (NaOH, 98%, flakes), and D-glucosamine hydrochloride ($C_6H_{13}NO_5 \cdot HCl$, > 98%, namely G in this work) were bought from Alfa Aesar, and hydrochloric acid (HCl, 37%) and sulfuric acid (H_2SO_4, 95%) were obtained from VWR Chemicals. All chemicals were used as received without further purification steps.

2.2. Synthesis

Two families of CMK-8-type NOMCs were prepared through the nanocasting method, starting from two different KIT-6 silica used as hard templates (namely, KIT-6_40 or KIT-6_100), which were synthesized with the same procedure described by Kleitz et al. [32], and hydrothermally treated at 40 °C for 72 h or at 100 °C for 48 h, respectively. NOMC samples were prepared by using a two-step impregnation procedure. The silica template was previously degassed overnight at 150 °C under vacuum; its pore volume value was used to determine the amount of the carbon source necessary to fulfill the porous template [33]. The relative amounts of glucosamine hydrochloride, water, and sulfuric acid were estimated from adjustments of a frequently used standard procedure for the impregnation with sucrose as the carbon source [33,34]. Precisely, for the first impregnation step, 1.0 g of glucosamine hydrochloride (G), 0.062 mL of H_2SO_4, and 4.0 g of doubly deionized water or 2.0 g of G, 0.123 mL of H_2SO_4, and 8.0 g of deionized water were used for each gram of KIT-6_40 or KIT-6_100, respectively. Glucosamine was previously dissolved in the sulfuric acid aqueous solution and was added dropwise to the silica powders. The mixture was stirred for 1 h at room temperature (RT) until a homogenous gel-like consistency was obtained. Then the slurry was thermally treated using three-step heating in a muffle furnace at 100 °C for 6 h, 140 °C for 2 h, and 160 °C for 6 h. The same procedure was repeated for the second impregnation step, reducing the initial amounts of reagents to 0.61 g of G, 0.038 mL of H_2SO_4, and 2.44 g of doubly deionized water or 1.22 g of G, 0.075 mL of H_2SO_4, and 4.88 g of doubly deionized water for KIT-6_40 or KIT-6_100 templates, respectively. The mixture was again treated at 100 °C for 6 h and 140 °C for 2 h in a muffle furnace. Then, each family of CMK-8 samples was pyrolyzed at three different temperatures: 600; 750; and 900 °C, for 4 h. The pyrolysis was carried out in a muffle furnace, using a quartz reactor with a capillary cap under atmospheric pressure [35]. The samples were heated from RT to the target pyrolysis temperature (T_p) (heating rate = 3 °C min^{-1}), with two intermediate steps at 200 °C for 6 h and at 655 °C for 4 h (the latter was absent on the samples pyrolyzed at 600 °C). Finally, the silica template was dissolved by stirring the carbonized powders overnight at RT in a 2 M NaOH water/ethanol solution (H_2O:ethanol = 1:1). A complete silica removal was accomplished by repeating this procedure three times (verified by the negligible amount of residual sample after thermogravimetric analysis [TGA]

under air). After that, the samples were washed several times in water and ethanol and dried overnight at 70 °C. For comparison purpose, another material was prepared with the same procedure, by using, in this case, sucrose (S) as the carbon source and KIT-6_100 as the hard template. The samples are named X_Y(Z), where X is the carbon source (G or S, respectively), Y the pyrolysis temperature (varying from 600 to 900 °C), and Z the temperature of the hydrothermal treatment of the silica template (i.e. 40 or 100 °C). For the courtesy of the reader, the list of the OMC samples synthesized in this work is summarized in Table 1.

2.3. Physicochemical characterization

A PANalytical Empyrean powder diffractometer equipped using the PIXcel^{3D} detector (Malvern PANalytical, the United Kingdom) was used for the low-angle X-ray diffraction (LAXRD) analysis. The LAXRD patterns were collected in transmission mode (using focusing mirror geometry) using a Cu K$\alpha_{1/2}$ radiation, at an operating voltage of 45.0 kV and a tube current of 40.0 mA. The measurements were carried out in continuous mode with a step size of $2\ \theta = 0.0131°$ and a data time per step of 50 s. High-resolution transmission electron microscopy (HR-TEM) images were taken using a Philips CM20 transmission electron microscope at an accelerating voltage of 200 keV in brightfield mode. For HR-TEM analysis, the samples were dispersed in ethanol via gentle sonication, and a droplet of the resulting mixture is deposited onto an aluminum TEM grid and dried at RT. The morphology of the materials was studied by Field Emission Scanning Electron Microscopy (FESEM) using a Zeiss Supra 40 microscope (Zeiss, Milano, Italy). The images were taken with magnifications from 1000 to 250,000 times at 5 kV. The samples for FESEM were prepared using the following procedure: the carbon powder is dispersed in ethanol, sonicated gently, and a droplet is deposited on a double-sided sticky carbon tape fixed to a flat sample holder and dried at RT. Specific surface area and porosity evaluation in the mesoporous range were carried out by N$_2$ adsorption-desorption measurements at 77 K (i.e. -196 °C), whereas microporosity was studied performing adsorption at 0 °C and using CO$_2$ as a gas probe. Adsorption-desorption of N$_2$ (at -196 °C) and CO$_2$ (at $-$ 10, 0, and 10 °C) was performed in an Anton Paar Quantatech Inc. IQ2 instrument (Boynton Beach, FL, USA). Before sorption analysis, silica and carbon samples were outgassed at 150 and 300 °C, respectively, for 12 h under vacuum. The calculations were carried out using the AsiQwin 5.2 software provided by Anton Paar Quantatech Inc. The specific surface area (S_{DFT}), pore size distribution (PSD), pore width (D_p), and pore volume ($V_{p,DFT}$) in the mesoporous range of silica samples were calculated using the non-local density functional theory (NLDFT) method, applied on the equilibrium branch of N$_2$ isotherms at -196 °C, considering an amorphous silica surface and a cylindrical pore model. The quench solid density functional theory (QSDFT) was used as a preferential method for the estimation of S_{DFT}, PSD, D_p, and $V_{p,DFT}$ of carbon samples. The QSDFT method was applied at the adsorption branch of N$_2$ isotherms at -196 °C,

considering the model for carbons and cylindrical pores as adsorbent and pore shape, respectively. The QSDFT method was chosen as the most accurate for this analysis because, with respect to NLDFT, it includes a roughness parameter, which takes into account the surface heterogeneity of some carbon materials [36]. Brunauer-Emmett-Teller (BET) surface area (S_{BET}) was also calculated adjusting opportunely the relative pressure of data point selection in the range $0.05 < p/p_0 < 0.2$. Micropore size distribution, pore width (D_{mp}) in the microporous range, micropore (V_{mp}, < 2 nm), and ultramicropore volume (V_{ump}, < 0.7 nm) were calculated from the adsorption branch of the CO$_2$ isotherms at 0 °C, using an NLDFT method specific for carbon surfaces. The isosteric enthalpy of adsorption (ΔH_{ads}) was calculated from the CO$_2$ adsorption branches of the isotherms obtained at three different temperatures, that is, -10, 0, and 10 °C, ($\Delta T = 10$ °C) and analyzed by the Clausius-Clapeyron approach using the software AsiQwin 5.2. The ΔH_{ads} values are derived from the slope of the Arrhenius plot (ln p vs. $^1/_T$), where p is the value of pressure at equal coverage, and T is the respective absolute temperature. Thermal degradation analysis was performed using a thermogravimetric analyzer NETZSCH TG 209 F3 Tarsus. An amount of 5−7 mg of the sample was burned in an alumina pan under airflow (20 mL min^{-1}) with N$_2$ as a protective gas (20 mL min^{-1}) in a temperature range of 30−800 °C (heating rate 10 °C min^{-1}). X-ray photoelectron spectroscopy (XPS, Nexsa, Thermo-Scientific, Massachusetts, USA) was performed using Al Kα radiation source operating at 72 W and an integrated flood gun. A pass energy of 200 eV, 'Standard Lens Mode,' CAE Analyzer Mode, and an energy step size of 1 eV for the survey spectrum were used. The diameter of the X-ray beam was 400 μm. Before analysis, the surface was cleaned by sputtering with Ar-clusters (1000 atoms, 6000 eV, 1 mm raster size) for 60 s. High-resolution spectra were acquired with 50 passes at a pass energy of 50 eV and an energy step size of 0.1 eV. High-resolution XPS spectra were fitted with Gaussian functions and a spline for the background subtraction using the software OriginPro 2020.

2.4. Pure CO$_2$ adsorption and CO$_2$/N$_2$ selectivity evaluation

The selectivity for CO$_2$ adsorption in a mixture with N$_2$ was evaluated by TGA on a NETZSCH TG 209 F1 Libra at 35 °C and ambient laboratory pressure ($\sim$ 1 bar). A schematic representation of the setup is shown in Figure S1 in the Supporting Information (SI). Before each test, to remove contaminants (mainly adsorbed gases or water) which can occlude the porosity, the samples were activated as follows: approximately 20 mg of the sample was activated with one cycle of vacuum and successively heating up to 500 °C for 15 min (heating rate 10 °C min^{-1}) under N$_2$ flow; when the temperature cooled down to 35 °C (cooling rate 40 °C min^{-1}), the sample was exposed to pure N$_2$ for 15 min, for stabilizing the weight. After that, a simulated flue gas [2] made up of 20 vol % of CO$_2$ and 80 vol % of N$_2$ (8 mL min^{-1} of CO$_2$ in a total flow of 40 mL min^{-1}) replaced N$_2$; the weight increase observed after the CO$_2$/N$_2$ gas mixture exposition for 120 min corresponds to the amount of CO$_2$ adsorbed by the sample.

Table 1
List of OMC samples synthesized in this work.

Sample name	Carbon source	Pyrolysis temperature, T_p (°C)	Hard template
G_600(40)	Glucosamine hydrochloride	600	KIT-6_40
G_750(40)	Glucosamine hydrochloride	750	KIT-6_40
G_900(40)	Glucosamine hydrochloride	900	KIT-6_40
G_600(100)	Glucosamine hydrochloride	600	KIT-6_100
G_750(100)	Glucosamine hydrochloride	750	KIT-6_100
G_900(100)	Glucosamine hydrochloride	900	KIT-6_100
S_900(100)	Sucrose	900	KIT-6_100

The desorption procedure was carried out in two stages: first, at the same temperature of 35 °C by sweeping the gas mixture for a pure N_2 flow for 1 h, to remove adsorbed CO_2; then, by heating the sample to 500 °C for 15 min (10 °C min^{-1}) for desorbing CO_2 adsorbed at the more energetic sites. Pure CO_2 and N_2 adsorption isotherms and cyclic CO_2 adsorption-desorption measurements were performed using a Surface Measurement System, Dynamic Vapor Sorption (DVS) instrument. The samples were activated under vacuum at 300 °C for 30 min before each analysis. The pure CO_2 and N_2 isotherms were carried out at a constant temperature of 30 °C while increasing the pressure up to 0.9 bar (10% of p/p_0 increase at each step). The equilibrium criterion condition for each step was chosen as $dm/dt = 0.002\%$ min^{-1}. Ideal adsorption solution theory (IAST) was applied on single-component adsorption isotherms of CO_2 and N_2 at 30 °C, from 0 to 90 kPa, accordingly to the methodology reported in the SI (see the Equations S1, S2, and S3). The molar fraction of the gas phase was chosen as 20% of CO_2 and 80% of N_2, as for the gas mixture measurements in TGA, or as 15% of CO_2 and 85% of N_2, as for more precise comparison with the majority of the literature reports. The affinity of CO_2 for the adsorbent surface was estimated by Henry's constant (K_H). K_H (mmol g^{-1} kPa^{-1}) was calculated from pure CO_2 adsorption isotherms at 0 °C in the limit of zero coverage using the virial isotherm model, as reported previously [37].

The reusability of the sorbents was tested with six consecutive adsorption-desorption cycles. Each adsorption step was performed at 0.2 bar and 30 °C (equilibrium criterion $dm/dt = 0.01\%$ min^{-1}). The desorption/regeneration step was carried out at 150 °C.
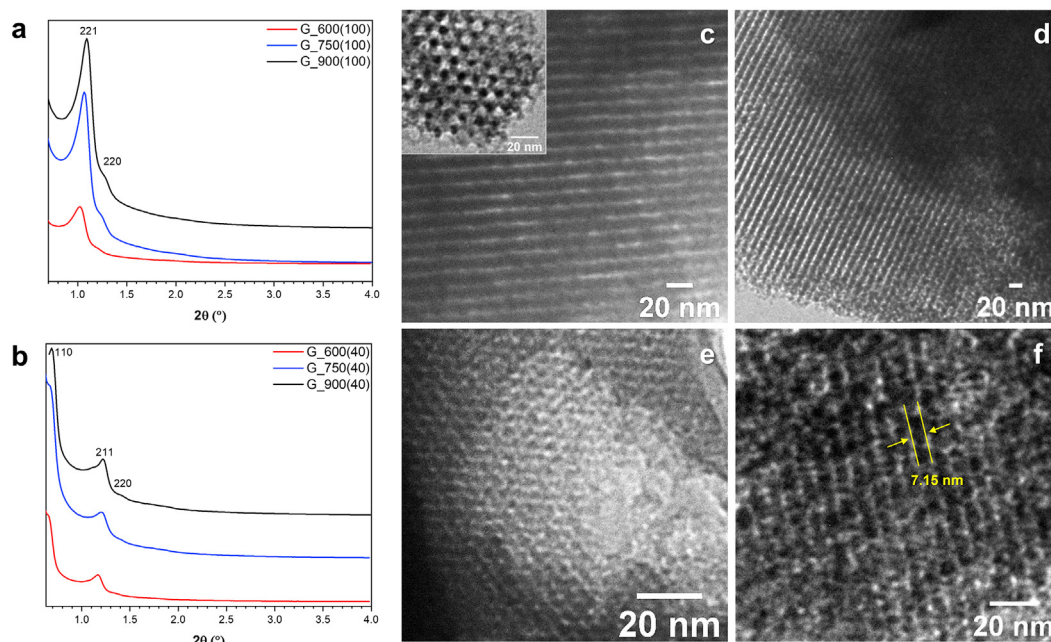
3. Results and discussion

3.1. Textural properties

Low-angle X-ray diffraction analysis (Fig. 1a and b), as a non-destructive method, was widely used to attain precise information about the structural attributes of the materials, chiefly the ordered arrangement in the mesoporous structures. The LAXRD diffraction pattern of KIT-6 silica is characteristic of cubic $Ia\bar{3}d$ symmetry (see Figures S2a and S3a in SI) [32]. The order mesoporous structure of the two families of carbon replicas is confirmed by both LAXRD and HR-TEM characterization techniques. In detail, X_Y(100) samples maintain the same $Ia\bar{3}d$ symmetry of the silica template, as demonstrated by the well-resolved (211) and (220) reflections in LAXRD patterns (see Fig. 1b and S4a). On the contrary, an additional diffraction peak at $2\theta < 1°$ indexed as (110) reflection [38] reveals a change in the symmetry for the G_Y(40) samples from the respective template (Fig. 1a). The lower symmetry of the mesostructure of this family of carbons has been explained by the absence of connectivity among the two mesoporous channel systems of KIT-6 when the hydrothermal treatment is performed at a temperature below 70 °C [39]. Their symmetry can be attributed to $I4_1/32$ [40], which is typically observed in CMK-1-type carbons, a carbon family derived from the replication of two pairs of non-interconnected pore systems of MCM-48 silica hard template [41]. The intensity and definition of LAXRD peaks increase as T_p increases, indicating a higher ordering in the mesoporous structure.

The HR-TEM images in Fig. 1c−f show the highly ordered porous structure of both the families of CMK-8 samples. X_Y(100) series of samples are characterized by a dense and interwoven framework (Fig. 1e and f and Figure S5 in SI), derived by the replication of both the two interconnected pore systems of KIT-6_100. On the contrary, G_Y(40) series of samples display disconnected framework systems that can be well distinguished in Fig. 1c and d. This observation corroborates the thesis of independent filling of the template porosity, typical for the replica from KIT-6_40 [42]. In addition, the FESEM images show a highly porous structure (Figure S6 in SI); in some areas of the samples, it is even possible to appreciate the ordered disposition of the pores.

The XRD unit cell size a_{211} was calculated from the (211) reflection using the expression $a_{211} = \sqrt{6} \cdot d_{211}$, where the
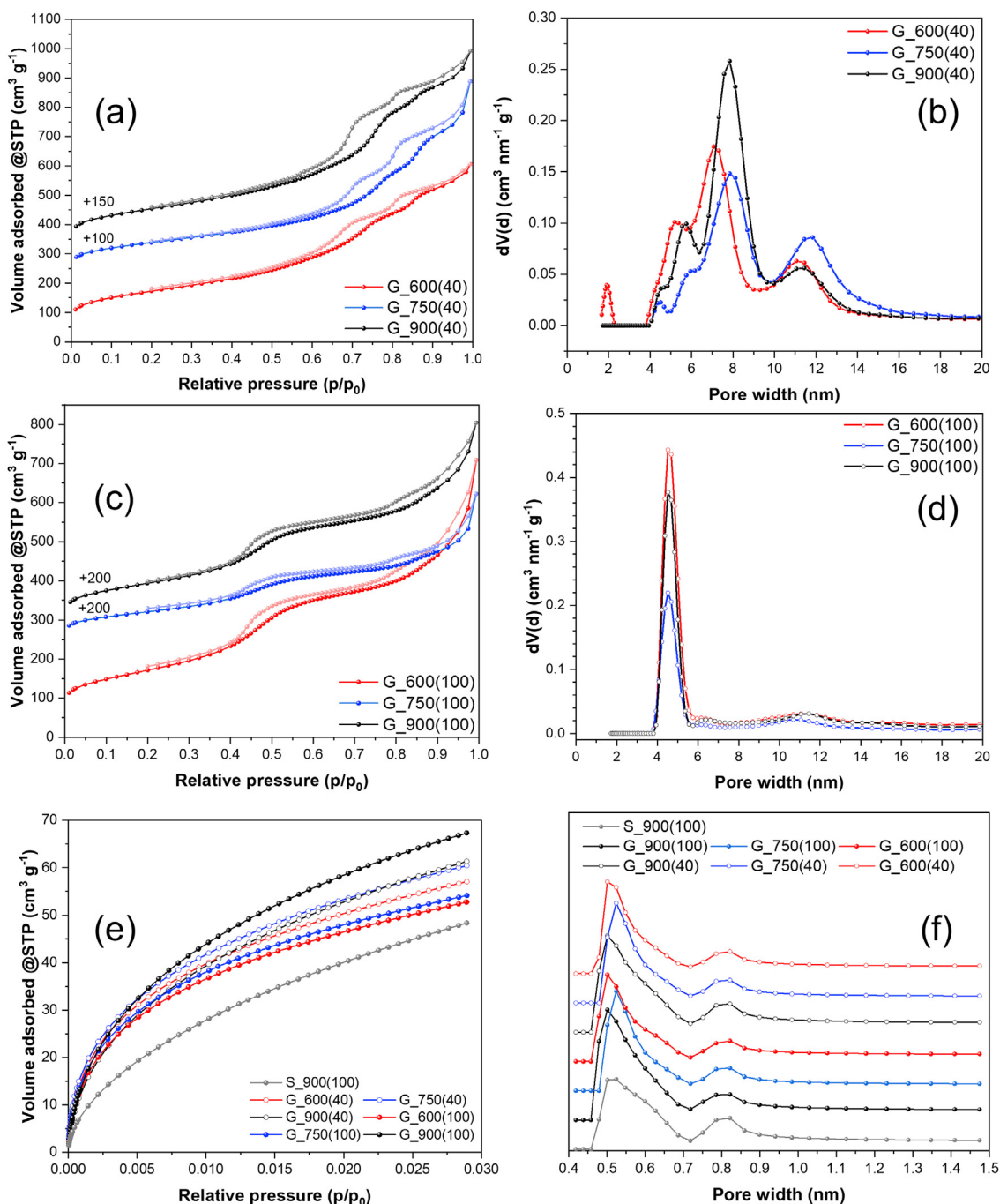

Fig. 1. Left hand-sided plots show LAXRD of NOMC samples obtained from glucosamine at different temperatures, namely, (**a**) G_600(40), G_750(40), G_900(40) and (**b**) G_600(100), G_750(100), and G_900(100) (red, blue, black lines, respectively). Right hand-sided images show HR-TEM micrographs of (**c**) G_600(40) with, in inset, insights into the ordered porous structure, (**d**) G_900(40), (**e**) G_600(100), and (**f**) G_900(100).

interplanar spacing d_{211} was calculated using the Bragg's law. The shrinkage of the mesostructure after the high-temperature treatment is observed by the decrease of the interplanar d-spacing and, consequently, of the unit cell size as T_p increases (Table S1).
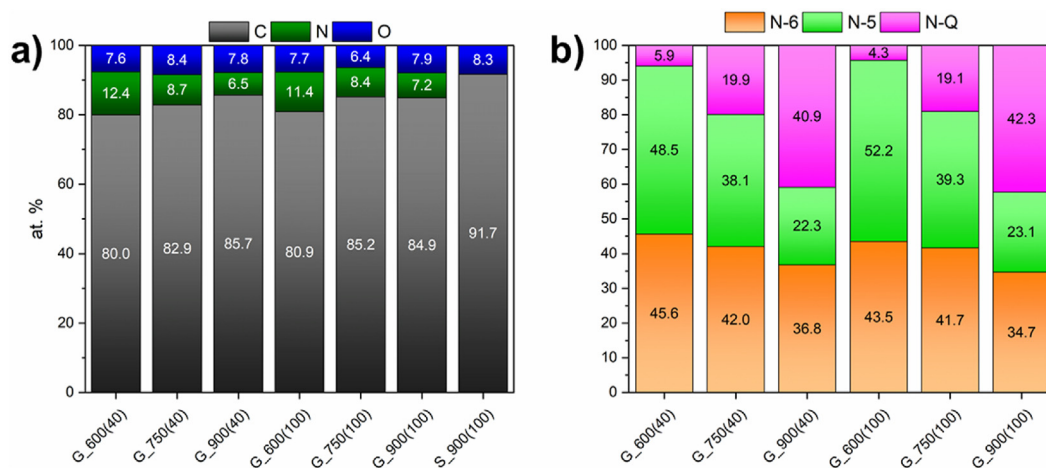
The porosity features were investigated by N_2 adsorption-desorption measurements at $-196\ °C$. All the samples show type IVa isotherms (IUPAC classification), which is typical of mesoporous materials like MCM-41 [43], with some character that resembles a type Ia isotherm (IUPAC classification), which is indicative of the presence of some micropores. The family of samples G_Y(40) has two hysteresis loops in the range $0.65 < p/p_0 < 0.85$, which correspond to a bimodal PSD (see Fig. 2a and b). The family of samples X_Y(100) has one hysteresis loop in the relative pressure range 0.4−0.8 and a PSD centered at 4.5 nm (Fig. 3c and d).

Besides the main population of pores, for both the G_Y(40) and G_Y(100) families of samples, an additional population of pores of

Fig. 2. N_2 adsorption-desorption isotherms at $-196\ °C$ and QSDFT pore size distributions of NOMC samples obtained from glucosamine at different temperatures: (**a** and **b**) G_600(40), G_750(40), and G_900(40) (red, blue, and black lines, respectively) and (**c** and **d**) G_600(100), G_750(100), and G_900(100) (red, blue, and black lines, respectively). CO_2 adsorption isotherms at $0\ °C$ (**e**) and NLDFT micropore size distributions (**f**) of OMC samples from glucosamine and sucrose: G_600(40); G_750(40); and G_900(40) (red, blue, and black empty dots, respectively) and G_600(100), G_750(100), G_900(100), and S_900(100) (red, blue, black, and gray full dots, respectively).

Fig. 3. a) Surface atomic ratio of C, N, and O as derived from XPS analysis of NOMCs prepared and under study in this work (see also Table S3 in SI); (**b**) relative ratio of the N-species (N-6, N-5, and N-Q) in G-derived NOMCs, as calculated from the deconvolution of the high-resolution XPS signals in the N1s region (full spectra are available in SI).

size around 11 nm is present, probably owing to incomplete pore filling [44]. Indeed, this population of larger pores is more evident for the replicas of the silica aged at 40 °C than for the one aged at 100 °C. This evidence can be again explained by the absence of interconnections between the two coupled sets of pores of KIT-6_40, which prevents the complete pore filling by the carbon source solution, or more precisely the filling of only one of the two-channel systems, leading to uncoupled subframework formation [45].

The specific surface area was calculated with both BET (S_{BET}) and QSDFT (S_{DFT}) methods. However, in the presence of microporosity, the BET method can be unreliable because it is difficult to distinguish between monolayer-multilayer adsorption and micropore filling [43]. For this reason, S_{DFT} is considered more reliable as the QSDFT method takes into account heterogeneity and surface roughness of carbon materials [46]. S_{DFT} increases at higher T_p, whereas the pore volume is not sensitively affected by the temperature of pyrolysis. V_{mp} increases with the increase of T_p owing to a more advanced pyrolytic degradation and reorganization of the carbon precursor and the release of small molecules with the increase of the temperature of pyrolysis [47]. It is also worthy to highlight that the bimodal micropore size distribution (see Fig. 2f) is composed of pores smaller than 1 nm, and the percentage of V_{ump} over V_{mp} is in the range of 63−70% for all the G-series of samples (56% for the S-derived sample), determined from the CO_2 adsorption-desorption isotherms at 0 °C (see Fig. 2e). The sample from sucrose has a lower specific surface area, and particularly

important for the application, a lower micropore content. The textural properties are summarized in Table 2. We can observe a good agreement between the pore diameters calculated from N_2 physisorption and from HR-TEM images (Fig. 2 and Tables 2 and S1). The wall thickness (b) was calculated using a geometrical model ($b = a_{211}/2 − D_{p,DFT}$) [39]. The parameter b decreases with the increase of the aging temperature for silica, which conversely reflects in thicker pore walls in the respective carbon replica. For carbon replicas, b decreases as long as T_p increases because of the phenomenon of framework shrinkage [48]. Silica template removal is considered to be successful as shown by the low residue observed after TGA analysis (Figure S7 in SI) and the low atomic percentage of Si (<1 at. %) from XPS survey analysis (Figure S8 and Table S2 in SI).

3.2. Physico-chemical properties

XPS analysis was performed to investigate the surface chemical composition and the bonding state. The surface atomic ratio of C, N, and O atoms was determined, and it is listed in Fig. 3a (and Table S3 in SI). The XPS regions of the previous elements were selected for high-resolution (HR) acquisitions to obtain semi-quantitative information based on peak areas and chemical information from the deconvolution into different chemically shifted components. Carbon signal was fitted by using three components (see Figures S9 and S12a in SI) assigned to C−C sp^2 (284.3−284.7 eV), C−O/C−N (285.9−286.5 eV),

Table 2
Physicochemical properties of the ordered mesoporous materials prepared and under study in this work.

Samples	a_{211}[a] (nm)	b[b] (nm)	S_{BET} (m^2 g^{-1})	S_{DFT} (m^2 g^{-1})	$V_{p,DFT}$ (cm^3 g^{-1})	D_p[c] (nm)	V_{ump} (cm^3 g^{-1})	V_{mp} (cm^3 g^{-1})	D_{mp}[d] (nm)
KIT-6_40	20.4	4.3	735	738	0.7	5.9	–	–	–
KIT-6_100	24.0	3.2	841	734	1.3	8.8	–	–	–
G_600(40)	18.6	3.1	619	779	0.9	5.2; 7.1	0.11	0.16	0.5; 0.8
G_750(40)	18.0	2.1	673	1043	0.9	5.8; 8.0	0.12	0.17	0.5; 0.8
G_900(40)	17.8	2.1	727	1062	1.0	5.8; 7.8	0.12	0.19	0.5; 0.8
G_600(100)	21.2	6.1	609	748	0.8	4.5	0.10	0.15	0.5; 0.8
G_750(100)	20.2	5.6	424	639	0.5	4.5	0.10	0.15	0.5; 0.8
G_900(100)	19.8	5.4	693	1069	0.8	4.5	0.13	0.22	0.5; 0.8
S_900(100)	19.4	5.0	673	783	0.8	4.7	0.09	0.16	0.5; 0.8

[a] Unit cell size (a_{211}) calculated using the expression $a_{211} = \sqrt{6} \cdot d_{211}$.
[b] Wall thickness (b) calculated by geometrical model, $b = a_{211}/2 − D_{p,DFT}$ [39].
[c] Pore width (D_p) in the mesoporous range, calculated by NLDFT and QSDFT methods for silica and carbons, respectively, applied to N_2 isotherms at −196 °C.
[d] Pore width (D_{mp}) of carbon samples in the microporous range, calculated by the NLDFT method applied to CO_2 isotherms at 0 °C.

and C=O/C=N (286.5−287.6 eV) [49,50]. Oxygen signal (Figures S10 and S12b in SI) was fitted by using three components assigned to C=O (∼ 531 eV), C−O (∼ 533 eV), and COOH (∼ 534 eV) [50]. The N bonding state was studied in relation to the pyrolysis temperature to understand the effect of the thermal treatment on the development of the different N species and their influence on CO_2 adsorption. The N1s signals of NOMCs were fitted by using three components assigned to pyridinic (N-6, 397.7−398.9 eV), pyrrolic (N-5, 399.9−400.7 eV), and graphitic (N-Q, 401.0−401.8 eV) nitrogen-based structures [49] (Figure S11 in SI) and graphically summarized in Fig. 3b. Accordingly, the fraction of N-5 decreases slightly when T_p increases from 600 to 750 °C, but it decreases dramatically at 900 °C. N-6 follows the same trend, even if the reduction is less appreciable. In contrast, N-Q is detected in a very low concentration in the sample pyrolyzed at 600 °C, but its relative amount increases with the increment of the pyrolysis temperature. Indeed, N-Q concentration is lower than 20% up to 750 °C but at 900 °C becomes the most abundant species. The evolution of nitrogen-containing moieties is ascribed to their different thermal stability. Particularly, N-5 is less stable than N-6 and N-Q at a higher temperature, as observed by Stańczyc et al. [51]. The surface atomic percentage of C and O/C and N/C ratio were plotted vs. the pyrolysis temperature in Figure S13. The surface C relative amount increases with the increment of the pyrolysis temperature as a consequence of the loss of heteroatoms [52]. In the T_p range 600−900 °C, the N/C content decreases, whereas O/C remains almost constant, consistently with the findings of Gehring et al. [52].

The thermal stability under air was assessed by TGA up to 800 °C. No significant weight loss is visible until 550−580 °C, therefore the samples are thermally stable under degassing conditions (500 °C in inert N_2 atmosphere, Figure S8 in SI), which is remarkable for an OMC material.

3.3. CO_2 adsorption measurements

The isosteric enthalpy of adsorption ΔH_{ads} and Henry's constant K_H were calculated from the adsorption isotherms in pure CO_2 to assess the intensity of the interaction between the gas and the adsorbents. ΔH_{ads} decreases as a function of surface coverage (Figure S14) because the adsorption occurs initially at the higher energy sites [53,54] and the steeper ΔH_{ads} drop is, the larger the energetic heterogeneity of the adsorption sites. ΔH_{ads} at low coverage lies in the range of 33−40 kJ mol^{-1} for all the samples, which is attributable to a physisorption mechanism (− 25 to − 50 kJ mol^{-1}) [55], then well-fitting with the range of 30−50 kJ mol^{-1} is considered optimal for a good balance between adsorption and ease of regeneration [56,57]. Henry's constant (K_H) and the virial coefficients C_1 e C_2 were also calculated from the CO_2 isotherms at 0 °C (Figure S15) and listed in Table S4 in SI. Sample S_900(100), lacking N, or the samples pyrolyzed at 900 °C show lower values of K_H compared with those pyrolyzed at 600−750 °C. This is the evidence of the relationship between the nitrogen content and the strength of CO_2-adsorbent interaction. The samples with a higher N content, particularly in the pyridinic form, have a higher K_H, because they can interact strongly with CO_2 [58].

A preliminary study of the sample performances was carried out from the observation of the adsorbed amounts in pure CO_2 at − 10, 0, and 10 °C at an absolute pressure up to 1 bar using a volumetric sorption analyzer. The amounts of CO_2 adsorbed by the samples at each temperature are reported in Table S5 in SI. G_900(100) shows the highest CO_2 adsorption capacity in these conditions associated with the highest micropore and ultra-micropore volumes. Differently, the N-lacking homologous S_900(100) sorbent has the lowest adsorption. This result confirms that the use of glucosamine as a carbon source instead of sucrose enhances the CO_2 uptake in this

family of ordered mesoporous materials, through the simultaneous increase of microporosity and nitrogen inclusion. Interestingly, the adsorption loss, observed by increasing the adsorption temperature from − 10 to 10 °C, follows the pyrolysis temperature order of 750 < 600 < 900 °C, and the highest drop is found in the S-derived sample. This observation suggests that the beneficial effect of nitrogen in improving CO_2 adsorption and selectivity gains a crucial role against microporosity at a temperature close to RT [59].

Similar results were achieved in pure CO_2 adsorption measurements at 30 °C and up to 90 kPa (0.9 bar) performed using a gravimetric sorption analyzer. A maximum weight increase of 6.5% (1.47 mmol g^{-1} of adsorbed CO_2) is achieved by sample G_900(100) at 90 kPa (Fig. 4). In general, the micropore and, in particular, the ultramicropore volume strongly influences pure CO_2 adsorption in the range of investigated temperatures [60].

To investigate the effect of the type and amount of N inclusions, but excluding the contribution of microporosity, the CO_2 adsorbed amount normalized over the micropore volume (CO_2 ads./V_{mp}, mmol cm^{-3}) was correlated with the overall XPS surface N content and each N species for all the G-derived samples, accordingly to the procedure already used by Sánchez-Sánchez et al. [59].

The experimental data were fitted with a linear function (see Fig. 5), and both the nature and the intensity of the contribution of each species in CO_2 adsorption were estimated from the slope of the trend line. Generally, we can state that the increment of the overall surface nitrogen content on the carbon surface has a beneficial effect, as indicated by the positive slope of the trend line (Fig. 5a) and in agreement with the results of Li et al. [26]. N-6 and N-5 enhance the CO_2 adsorption (Fig. 5b and c), even if to a different extent. Indeed, from the comparison of the values of the slopes, both N-5 and N-6 positively participate in the CO_2 adsorption, but the highest contribution to the adsorption is owing to N-6. N-6 and N-Q interact more easily with CO_2 owing to their higher basicity compared with pyrrolic moieties [61]. N-5 promotes the adsorption of CO_2 through hydrogen-bonding-like interactions occurring between the positively charged hydrogen bonded to the nitrogen atom of the pyrrolic moiety and the oxygen atom of CO_2 [62], which is a weaker interaction than the Lewis acid-base one occurring in N-6 and N-Q [61].

As reported by Lim et al. [61], CO_2 is adsorbed onto the surface of quaternary nitrogen-containing carbon with an angle of up to 179.93, whereas the presence of N-5 structures leads to the alignment of CO_2 and N−H on an axis. Accordingly, this last interaction
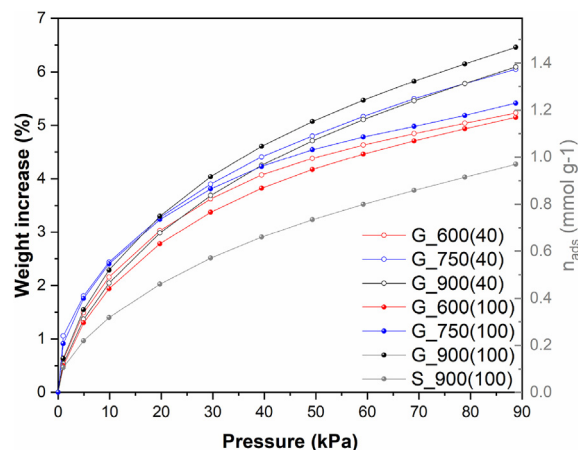

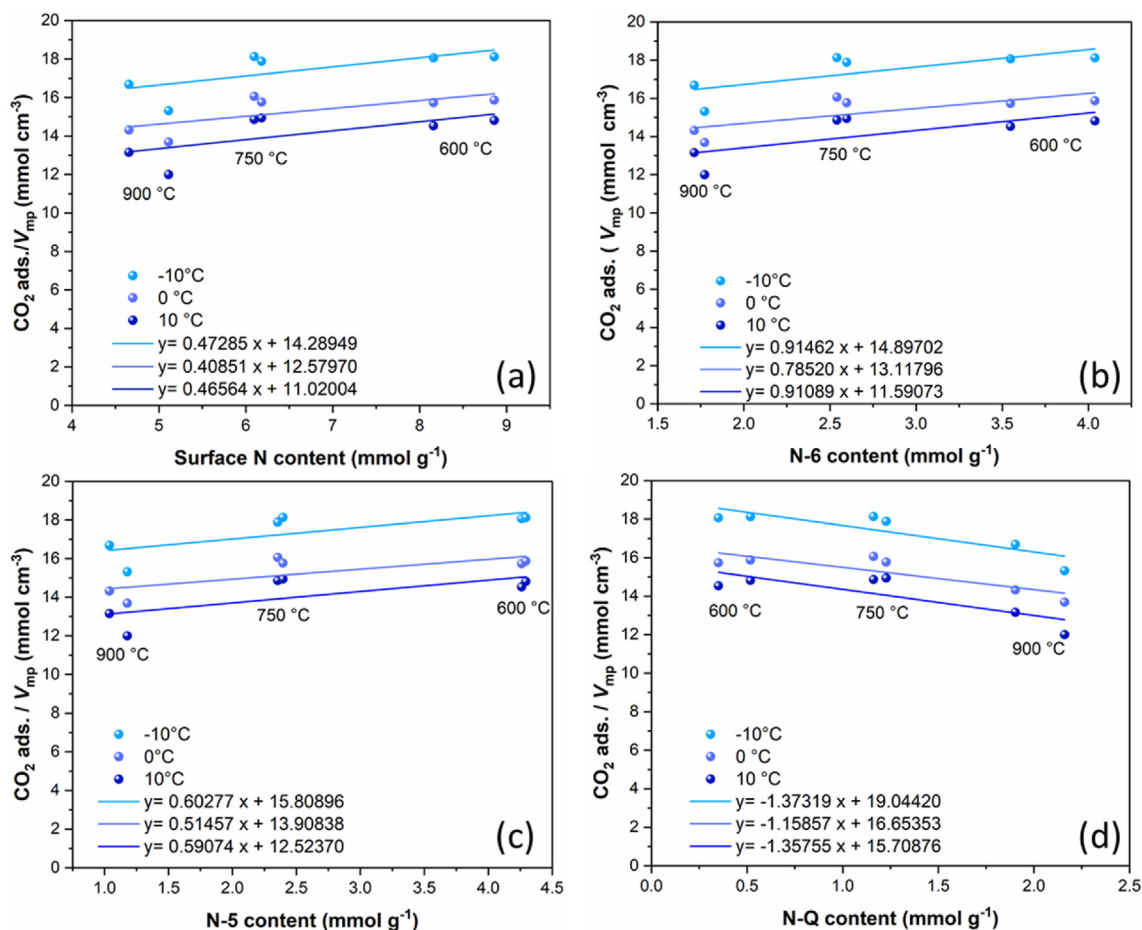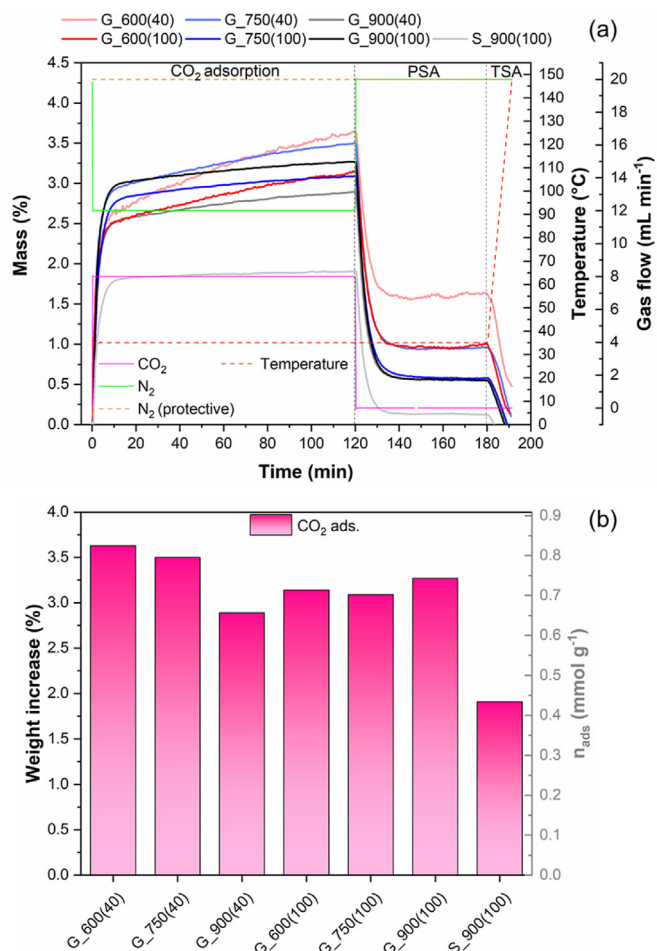**Fig. 4.** Pure CO_2 adsorption at 30 °C up to 90 kPa performed using a gravimetric sorption analyzer.

Fig. 5. Dependence of CO_2 normalized adsorption with overall surface N (**a**), N-6 (**b**), N-5(**c**), and N-Q (**d**) content.

(H-bonding) prevents an efficient $\pi-\pi$ stacking between CO_2 and the graphitic carbon orbital system owing to geometrical constrains as occurs in the case of N-Q. In principle, also N-Q should increase the affinity for CO_2 when compared with the bare carbon surface [62]. However, in this specific case, CO_{2ads}/V_{mp} decreases with the increase of N-Q (Fig. 5d), which is likely ascribed to the less abundant total concentration (mmol g^{-1}) of N-Q species when compared with N-5 and N-6. Moreover, the N-Q concentration increase is related to the decrease of N-6 and N-5, which contributes to CO_2 adsorption in a stronger or comparable extent, respectively [61]. Nevertheless, the highest concentration of N-Q coincides with the higher content of micropores and ultra-micropores, which strongly contributes to CO_2 adsorption, particularly at lower temperature. The simultaneous presence of both nitrogen and oxygen atoms could also positively affect the CO_2 adsorption performances of the material [63]. The interaction mechanism during the CO_2 adsorption is mainly owing to the dipolar interactions as in the case of nitrogen-based materials even if the adsorption is mainly owing to nitrogen species, as previously reported by Wu et al. [64].

TGA measurement was performed at 35 °C and 1 bar exposing the samples to a mixture composed of 20 vol% CO_2 and 80 vol % of N_2 to evaluate the competitive adsorption of these two gases; results are shown in Fig. 6a and b. Temperature and gas composition conditions were chosen to be similar to a typical exhaust gas [65]. The condition scheme used to perform these experiments is shown in Figure S1 in SI. The observed sample weight increase is related to CO_2 adsorption (Fig. 6b and Table 3). However, the amount of adsorbed CO_2 in these conditions is lower if compared with the

values obtained on the measurements performed under pure CO_2. The generic decrease of CO_2 adsorption is ascribed to both the increase of the tested temperature, typically observed for a physisorption process [25], to the lower partial pressure of CO_2 in the gas flow, and to the slight amount of adsorbed nitrogen considered in the initial mass, that will be partially replaced by CO_2 owing to the preferential adsorption of CO_2 as compared with N_2. The beneficial effect of nitrogen content in carbon samples is more significant when adsorption occurs at higher temperature and in a mixed CO_2/N_2 gas atmosphere. Indeed, G_600(Z) and G_750(Z) samples here match or outperform G_900(Z) series of samples, which in contrast demonstrated enhanced performance under pure CO_2 adsorption conditions in the temperature range from − 10 to 30 °C. The improved selectivity is attributed to the higher surface N content and, particularly, to the superior concentration of pyridinic-N inclusions. Lim et al. [61] actually demonstrated that N-6 is particularly effective in selective adsorption, not only for the strong affinity for CO_2 but also for the high adsorption energy difference between CO_2 and N_2. Indeed, higher CO_2 adsorption values, equal to 3.6 and 3.5% weight increase (0.82 and 0.80 mmol g^{-1}, respectively), are reached by the samples G_600(40) and G_750(40), respectively, which in these conditions outperform G_900(100), being the most performing sample in pure CO_2. N-lacking sample S_900(100) again shows the lowest performance in terms of CO_2 adsorption and selectivity. The adsorbed amounts and the percentage of released CO_2 in pressure swing adsorption (PSA) conditions are listed in Table 3. The adsorption capacity and selectivity results are consistent with the calculated K_H values (see

Fig. 6. (**a**) Adsorption and desorption steps for CO_2/N_2 adsorption measurements of NOMCs under study and (**b**) weight increase owing to CO_2 adsorption in a gas mixture of 20 vol % CO_2 and 80 vol % of N_2 at 35 °C. Details on setup for CO_2/N_2 selectivity tests by TGA in Figure S1 in SI.

Table S4) in SI). It is interesting to observe that almost all the adsorbed CO_2 is released in PSA (Fig. 6a), that is, only exposing the sample to a flow of N_2 without heating. The percentage of CO_2 released under PSA conditions appears to be inversely related to N content. Then, heating was applied to remove CO_2 adsorbed in the most energetic sites. At temperatures <150 °C, most of the adsorbed CO_2 is released.

To properly compare our work with other literature reports, the CO_2/N_2 selectivity on the most selective sample (viz., G_600(40)) was also evaluated as per the widely used IAST. Single-component adsorption isotherms of CO_2 and N_2 were performed in the same condition (at 30 °C, from 0 to 90 kPa) (see Fig. 7a).

As can be observed from the isotherms in Fig. 7a, the N_2 adsorbed amount is much lower than the CO_2 one in the whole pressure range (0.20 and 1.18 mmol g^{-1} at 90 kPa, respectively); this confirms the high CO_2/N_2 selectivity of the G-series of samples. S_{IAST} calculated on the G_600(40) sample lays in the range 37-24 (for a gas mixture composed of $CO_2/N_2 = 20:80$, see Fig. 7b) or 52-34 (for a gas mixture composed of $CO_2/N_2 = 15:85$, see Figure S16 in SI) in the tested pressure range (0−90 kPa).
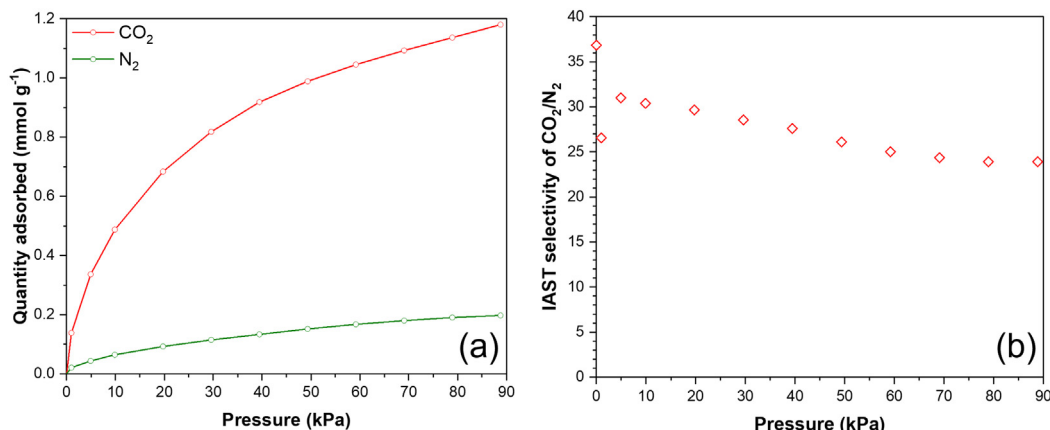
Reusability of the sorbents was assessed by pure CO_2 adsorption measurements at 30 °C and at 20 kPa (0.2 bar), regenerating the sorbents under temperature swing adsorption (TSA) conditions, by heating up to 150 °C between two consecutive cycles (Fig. 8a). Generally, the highest loss in adsorption performances (see Fig. 8b) occurs between the first and the second cycle, thus a certain

amount of CO_2 cannot be desorbed at 150 °C, likely because strongly bonded or remained trapped inside the narrowest micropores. After the second cycle, the adsorbed amount is almost unvaried, proving that the sorbents can be reused without losing their performances and, in addition, be sufficiently regenerated under mild conditions.

To enlighten even more the quality and positive characteristics of the glucosamine-derived NOMCs prepared and characterized in this work, we here compare their performances with the most significant literature reports (see Table 4), which we consider to be similar in terms of overall physicochemical features and comparable chiefly in terms of selective CO_2 adsorption in CO_2/N_2 gas mixtures. The first three entries of Table 4 refer to OMCs/NOMCs developed in this work, namely, the undoped carbon sample S_900(100), and the most performing NOMCs in terms of pure CO_2 adsorption or CO_2/N_2 separation, viz. G_900(100) or G_600(40), respectively. It is worth noticing here that, owing to the heterogeneity of the testing conditions, we found it difficult to carry out a direct comparison among all the literature reports; actually, although a reliable evaluation of separation ability should be realized via gas mixture measurements [66], most of the research articles determine selectivity using single-component adsorption isotherms, by Henry's constant ratio, initial slopes (IS) of the adsorption isotherms (see references [[67]), or the IAST (see references [68−71]). In terms of testing conditions, a complete comparison can be performed only with the work of García-Díez et al. [25]: both the NOMC samples developed in our work demonstrate slightly enhanced selectivity in CO_2/N_2 mixtures (20/80 v/v) [25]. Remarkably, in our work, adsorption is performed at a higher temperature (35 °C vs. 25 °C in the literature counterpart), and no post-treatments for porosity modification are carried out. However, to allow a wider comparison with most literary works, S_{IAST} was calculated for the sample G_600(40) in a gas mixture composed of 15% of CO_2 and 85% of N_2 (see Figure S16 in SI). The most selective sample synthesized in our work (viz. G_600(40)) reports S_{IAST} within the range of 52-34 (0−90 kPa), perfectly in agreement with the works of Vorokhta et al. [68], Wan et al. [69] and Liu et al. [71] included in our comparison. In terms of pure CO_2 adsorption, even if this condition does not represent the key purpose of our work, G_900(100) shows comparable CO_2 adsorbed amounts under similar adsorption conditions compared with the sample a-NOMC reported by Chang et al. [30]. Anyway, in the latter literature report [30], nitrogen groups were introduced via ammonia heat treatment and amine refluxing, whereas in this work, no post-treatments are carried out. Samples OMC-20-80-24-700 [67], NOMC-L-0.5 [69], CN-0.45 [28], 0.52@PEI-AOMC [70], CMK-3 [68] and N-OMC-750 [71] seem to outperform our synthesized OMCs/NOMCs in terms of pure CO_2 adsorption. However, as a general drawback, the previously cited studies used toxic carbon sources and/or additional activation steps for the adjustment of microporosity. On the contrary, here we show that adsorbents with abundant and tailored porosity can be readily prepared by the nanocasting procedure, without requiring any further activation

Table 3
Adsorption and desorption analysis of mixed CO_2/N_2 adsorption tests by TGA.
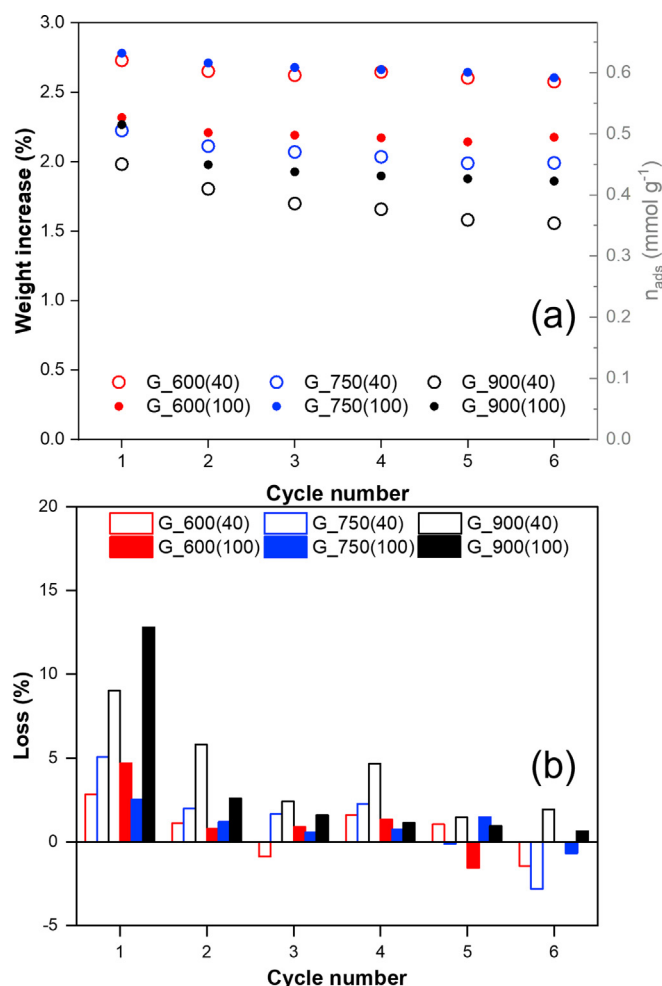
Samples	Mass change (%)	CO_2 ads (mmol g^{-1})	Released CO_2 in PSA (%)
G_600(40)	3.6	0.82	55.6
G_750(40)	3.5	0.80	72.6
G_900(40)	2.9	0.66	80.3
G_600(100)	3.1	0.71	67.8
G_750(100)	3.1	0.70	81.2
G_900(100)	3.3	0.74	82.9
S_900(100)	1.9	0.43	93.7

Fig. 7. (**a**) CO_2 and N_2 adsorption isotherms at 30 °C and (**b**) IAST-predicted selectivity for a gas mixture composed of 20 vol % CO_2 and 80 vol % of N_2 for the sample G_600(40). Details on S_{IAST} calculation in SI.

steps. Moreover, glucosamine hydrochloride, acting concurrently as both the carbon and the nitrogen source, allows the direct incorporation in a single step of the crucial N functionalities, bypassing

Fig. 8. Reusability tests of G-series of NOMCs under repetitive adsorption (30 °C) - desorption (150 °C) cycles at 0.2 bar: (**a**) amount of CO_2 adsorbed and (**b**) regeneration efficiency over cycling.

time/energy consuming ammonia post-treatments or amine refluxing processes. Glucosamine hydrochloride itself is a non-toxic and potential natural occurring source of carbon; hence, it shows highly promising prospects as a suitable raw material for biomass valorization in a circular economy loop. Finally, it is fair to underline that in this work the activation step before CO_2 adsorption measurements is performed at a higher temperature compared with the studies listed in Table 4. Therefore, regeneration conditions can be considered as a margin for improvement in this research, to make sorbents reuse more feasible from the energy consumption point of view.

4. Conclusions

D-glucosamine hydrochloride was successfully explored for the first time as a sustainable C/N precursor for the synthesis of NOMCs obtained through the nanocasting technique and specifically conceived for selective CO_2 adsorption. The applied method enabled the accurate design of the pore characteristics through the convenient choice of the KIT-6 silica hard templates and the adjustment of the carbonization process. The effect of the pyrolysis temperature on the development of microporosity and of the different types of nitrogen inclusions was also accurately investigated. XPS analysis was used to identify the nitrogen species (pyridinic, pyrrolic, and graphitic nitrogen-based structures), which were formed during the thermal treatment; their respective contribution on CO_2 adsorption and selectivity in CO_2/N_2 mixtures (20/80 v/v) was investigated.

The obtained results revealed that an enhanced micropore content, related to the higher pyrolysis temperature (900 °C), was effective in enhancing adsorption capacity in pure CO_2 flow. On the contrary, the lower pyrolysis temperature (600 °C) allowed for the retention of a higher amount of N inclusions in the carbon framework, mainly in the form of pyrrolic-N and pyridinic-N, the latter being particularly beneficial for improving the selective adsorption of CO_2. Specifically, a maximum CO_2 adsorption capacity of 1.47 mmol g^{-1} was achieved by the sample G_900(100) at 30 °C/ 0.9 bar/pure CO_2, whereas a CO_2 uptake of 0.82 mmol g^{-1} was obtained by the sample G_600(40) at 35 °C/1 bar/20% CO_2. In addition, reusability tests remarkably showed good capacity retention on reversible and repetitive adsorption-desorption cycles. The maximum adsorption loss was registered between the first and the second cycle, which was ascribed to an insufficient

Table 4
Comparison of the performance in terms of CO_2/N_2 separation of OMCs/NOMCs developed in this work with the most significant literature reports.[b,c,d,e,f,g,h,i,j,k,l,m]

Materials [REF]	Samples [REF]	Synthesis	Precursors	N content %	CO_2 capacity mmol·g^{-1}	Selectivity CO_2:N_2	T_{ads} °C	P_{ads} bar	T_{act} °C
OMC [this work]	S_900(100)	H.T.[f]	Sucrose	—	0.43 (CO_2:N_2 = 20:80)	—	35	1	300
					0.97 (100% CO_2)	—	30	0.9	
NOMC [this work]	G_900(100)	H.T.[f]	Glucosamine hydrochlor.	7.2[a]	0.74 (CO_2:N_2 = 20:80)	—	35	1	300
					1.47 (100% CO_2)	—	30	0.9	
NOMC [this work]	G_600(40)	H.T.[f]	Glucosamine hydrochlor.	12.4[a]	0.82 (CO_2:N_2 = 20:80)	—	35	1	300
					1.18 (100% CO_2)	52:1−34:1[c] (CO_2:N_2 = 15:85)	30	0.9	
NOMC (CMK-3) [25]	OMCreo CA 4:1850	H.T.[f] + C.A.[g]	Creosote	0.37[b]	~0.7 (CO_2:N_2 = 20:80)	—	25	1	120
	OMCreo Pat 48%	H.T.[f] + P.A.[h]		2.39[b]	~0.6 (CO_2:N_2 = 20:80)	—			
OMC (CMK-3) [68]	CMK-3	H.T.[f]	Furfuryl alcohol	—	1.7 (100% CO_2)		20	1	200
					—	35.2:1−38:1[c] (CO_2:N_2 = 15:85)	20−50		
Single crystal NOMC [67]	OMC-20-80-24-700	One-pot self-assembly	Resorcinol, HMT[j], urea, ammonia	0.78[a]	2.78 (100% CO_2)	29:1[d]	25	1	200
NOMC [69]	NOMC-L-0.5	S.T.[i]	Resorcinol, 3-aminophenol, l-lysine	2.5[a]	2.50 (100% CO_2)	43:1[c] (CO_2:N_2 = 15:85)	25	1	120
NOMC [30]	a-N-OMC	S.T.[i]	Sucrose, ammonia, TEPA[k]	2.56[b]	1.41 (100% CO_2)	m.i.[e] (CO_2:N_2 = 10:90)	35	1	120
NOMC [28]	CN-0.45	S.T.[i]	Resorcinol, HMT[j], EDA[l]	2.97[b]	2.71 (100% CO_2)	28:1[d]	25	0.95	150
NOMC [70]	0.52@PEI-AOMC	S.T.[i]	Phloroglucinol formaldehyde resol, PEI[m]	21.58[b]	2.58 (100% CO_2)	64:1[c] (CO_2:N_2 = 10:90)	30	1	180
NOMC [71]	N-OMC-750	S.T.[i]	Terephthalaldehyde, m-aminophenol, F127, urea	6.53[b]	1.64 (100% CO_2)	54.0:1[c] (CO_2:N_2 = 15:85)	25	0.15	150

[a] Determined by XPS (at. %).
[b] Determined by elemental analysis (wt. %).
[c] Determined by ideal adsorption solution theory (IAST) method.
[d] Determined by initial slope (IS) method.
[e] m.i. denotes missing information.
[f] H.T. is for hard template.
[g] C.A. is for chemical activation.
[h] P.A. is for physical activation.
[i] S.T. is for soft templating.
[j] HMT is for hexamethylenetetramine.
[k] TEPA is for tetraethylenepentamine.
[l] EDA is for ethylenediamine.
[m] PEI is for poly(ethyleneimine).

regeneration temperature (150 °C) rather than an efficiency loss by the adsorbents.

In summary, the use of glucosamine hydrochloride as an environmentally friendly carbon/nitrogen source enabled the preparation of selective and high-performing ordered mesoporous CO_2 adsorbents, with remarkable features of sustainability and regenerability. The newly developed NOMCs outperformed the undoped analogs obtained from sucrose and are amongst the most significant literature reports, chiefly in terms of selective CO_2 adsorption. The obtained results demonstrate that proper combination of the suitable C/N precursors, the synthesis conditions, and the pore architecture are highly effective in obtaining high performing, sustainable, and reusable CO_2 sorbents, without any need for time/energy consuming activation steps or N-doping post-treatments.

Funding sources

Credit author statement

Conceptualization: E.M.; M.A.O.L.; S.B.; F.K.; C.G. data acquisition and curation: E.M.; M.A.O.L.; T.P.; M.B. investigation and methodology: E.M.; M.A.O.L.; T.P.; M.B. writing - original draft: E.M.; M.B. writing - review and editing: all authors. Funding and resources: C.F.P.; G.S.; F.K.; C.G. Supervision: C.F.P.; S.B.; F.K. C.G. All authors have read and agreed to the published version of the article.

Declaration of competing interest

The authors declare that they have no known competing financial interests or personal relationships that could have appeared to influence the work reported in this article.

Acknowledgment

Appendix A. Supplementary data

Supplementary data to this article can be found online at https://doi.org/10.1016/j.mtsust.2021.100089.

References

[1] WMO - World Meteorological Organization, Global climate report - August 2020 | state of the climate. https://www.ncdc.noaa.gov/sotc/global/202008, 2020.

[2] A. Sayari, Y. Belmabkhout, R. Serna-Guerrero, Flue gas treatment via CO2 adsorption, Chem. Eng. J. 171 (2011) 760−774, https://doi.org/10.1016/j.cej.2011.02.007.

[3] J. Gibbins, H. Chalmers, Carbon capture and storage, Energy Pol. 36 (2008) 4317−4322, https://doi.org/10.1016/j.enpol.2008.09.058.

[4] B.K. Choi, S.M. Kim, K.M. Kim, U. Lee, J.H. Choi, J.S. Lee, I.H. Baek, S.C. Nam, J.H. Moon, Amine blending optimization for maximizing CO2 absorption capacity in a diisopropanolamine − methyldiethanolamine − H2O system using the electrolyte UNIQUAC model, Chem. Eng. J. 419 (2021) 129517, https://doi.org/10.1016/j.cej.2021.129517.

[5] E. Davarpanah, S. Hernández, G. Latini, C.F. Pirri, S. Bocchini, Enhanced CO2 absorption in organic solutions of biobased ionic liquids, Adv. Sustain. Syst. 4 (2020) 1−8, https://doi.org/10.1002/adsu.201900067.

[6] Y. Bi, Z. Hu, X. Lin, N. Ahmad, J. Xu, X. Xu, Efficient CO2 capture by a novel deep eutectic solvent through facile, one-pot synthesis with low energy consumption and feasible regeneration, Sci. Total Environ. 705 (2020) 135798, https://doi.org/10.1016/j.scitotenv.2019.135798.

[7] L. Nie, Y. Mu, J. Jin, J. Chen, J. Mi, Recent developments and consideration issues in solid adsorbents for CO2 capture from flue gas, Chin. J. Chem. Eng. 26 (2018) 2303−2317, https://doi.org/10.1016/j.cjche.2018.07.012.

[8] C.A. Scholes, S.E. Kentish, A. Qader, Membrane gas-solvent contactor pilot plant trials for post-combustion CO2 capture, Separ. Purif. Technol. 237 (2020) 116470, https://doi.org/10.1016/j.seppur.2019.116470.

[9] Z. Liao, Y. Hu, J. Wang, Y. Yang, F. You, Systematic design and optimization of a membrane-cryogenic hybrid system for CO2 capture, ACS Sustain. Chem. Eng. 7 (2019) 17186−17197, https://doi.org/10.1021/acssuschemeng.9b03727.

[10] F. Hussin, M.K. Aroua, Recent trends in the development of adsorption technologies for carbon dioxide capture: a brief literature and patent reviews (2014−2018), J. Clean. Prod. 253 (2020) 119707, https://doi.org/10.1016/j.jclepro.2019.119707.

[11] A. Mukherjee, J.A. Okolie, A. Abdelrasoul, C. Niu, A.K. Dalai, Review of post-combustion carbon dioxide capture technologies using activated carbon, J. Environ. Sci. (China) 83 (2019) 46−63, https://doi.org/10.1016/j.jes.2019.03.014.

[12] Z. Qiang, R. Li, Z. Yang, M. Guo, F. Cheng, M. Zhang, Zeolite X adsorbent with high stability synthesized from bauxite tailings for cyclic adsorption of CO2, Energy Fuel 33 (2019) 6641−6649, https://doi.org/10.1021/acs.energyfuels.9b01268.

[13] H. Li, K. Wang, Z. Hu, Y.P. Chen, W. Verdegaal, D. Zhao, H.C. Zhou, Harnessing solvent effects to integrate alkylamine into metal-organic frameworks for exceptionally high CO2 uptake, J. Mater. Chem. A. 7 (2019) 7867−7874, https://doi.org/10.1039/c8ta11300a.

[14] J.A. Cecilia, E. Vilarrasa-García, R. Morales-Ospino, M. Bastos-Neto, D.C.S. Azevedo, E. Rodríguez-Castellón, Insights into CO2 adsorption in amino-functionalized SBA-15 synthesized at different aging temperature, Adsorption 26 (2020) 225−240, https://doi.org/10.1007/s10450-019-00118-1.

[15] W. Hui, X.M. He, X.Y. Xu, Y.M. Chen, Y. Zhou, Z.M. Li, L. Zhang, D.J. Tao, Highly efficient cycloaddition of diluted and waste CO2 into cyclic carbonates catalyzed by porous ionic copolymers, J. CO2 Util. 36 (2020) 169−176, https://doi.org/10.1016/j.jcou.2019.11.003.

[16] B. González, J.J. Manyà, Activated olive mill waste-based hydrochars as selective adsorbents for CO2 capture under postcombustion conditions, Chem. Eng. Process. - Process Intensif. 149 (2020) 107830, https://doi.org/10.1016/j.cep.2020.107830.

[17] Z. Zhang, Z.P. Cano, D. Luo, H. Dou, A. Yu, Z. Chen, Rational design of tailored porous carbon-based materials for CO2 capture, J. Mater. Chem. A. 7 (2019) 20985−21003, https://doi.org/10.1039/c9ta07297g.

[18] P.D. Dissanayake, S. You, A.D. Igalavithana, Y. Xia, A. Bhatnagar, S. Gupta, H.W. Kua, S. Kim, J.H. Kwon, D.C.W. Tsang, Y.S. Ok, Biochar-based adsorbents for carbon dioxide capture: a critical review, Renew. Sustain. Energy Rev. 119 (2020) 109582, https://doi.org/10.1016/j.rser.2019.109582.

[19] R. Ben-Mansour, M.A. Habib, O.E. Bamidele, M. Basha, N.A.A. Qasem, A. Peedikakkal, T. Laoui, M. Ali, Carbon capture by physical adsorption: materials, experimental investigations and numerical modeling and simulations - a review, Appl. Energy 161 (2016) 225−255, https://doi.org/10.1016/j.apenergy.2015.10.011.

[20] G. Sethia, A. Sayari, Comprehensive study of ultra-microporous nitrogen-doped activated carbon for CO2 capture, Carbon N. Y. 93 (2015) 68−80, https://doi.org/10.1016/j.carbon.2015.05.017.

[21] V. Presser, J. McDonough, S.H. Yeon, Y. Gogotsi, Effect of pore size on carbon dioxide sorption by carbide derived carbon, Energy Environ. Sci. 4 (2011) 3059−3066, https://doi.org/10.1039/c1ee01176f.

[22] J. Zhou, X. Wang, W. Xing, Carbon-based CO2 Adsorbents, The Royal Society of Chemistry, 2019.

[23] R.B. Vieira, P.A.S. Moura, E. Vilarrasa-García, D.C.S. Azevedo, H.O. Pastore, Polyamine-grafted magadiite: high CO2 selectivity at capture from CO2/N2 and CO2/CH4 mixtures, J. CO2 Util. 23 (2018) 29−41, https://doi.org/10.1016/j.jcou.2017.11.004.

[24] M. Vorokhta, J. Morávková, D. Řimnáčová, R. Pilař, A. Zhigunov, M. Švábová, P. Sazama, CO2 capture using three-dimensionally ordered micromesoporous carbon, J. CO2 Util. 31 (2019) 124−134, https://doi.org/10.1016/j.jcou.2019.03.001.

[25] E. García-Díez, A. Castro-Muñiz, J.I. Paredes, M.M. Maroto-Valer, F. Suárez-García, S. García, CO2 capture by novel hierarchical activated ordered micromesoporous carbons derived from low value coal tar products, Microporous Mesoporous Mater. 318 (2021), https://doi.org/10.1016/j.micromeso.2021.110986.

[26] J. Li, M. Hou, Y. Chen, W. Cen, Y. Chu, S. Yin, Enhanced CO 2 capture on graphene via N, S dual-doping, Appl. Surf. Sci. 399 (2017) 420−425, https://doi.org/10.1016/j.apsusc.2016.11.157.

[27] B. Petrovic, M. Gorbounov, S. Masoudi Soltani, Influence of surface modification on selective CO2 adsorption: a technical review on mechanisms and methods, Microporous Mesoporous Mater. 312 (2021) 110751, https://doi.org/10.1016/j.micromeso.2020.110751.

[28] J.H. Yu, J.H. So, Synthesis and characterization of nitrogen-containing hydrothermal carbon with ordered mesostructure, Chem. Phys. Lett. 716 (2019) 237−246, https://doi.org/10.1016/j.cplett.2018.12.014.

[29] G. Singh, R. Bahadur, J. Mee Lee, I. Young Kim, A.M. Ruban, J.M. Davidraj, D. Semit, A. Karakoti, A.H. Al Muhtaseb, A. Vinu, Nanoporous activated biocarbons with high surface areas from alligator weed and their excellent

performance for CO2 capture at both low and high pressures, Chem. Eng. J. 406 (2021), https://doi.org/10.1016/j.cej.2020.126787.

[30] R.W. Chang, C.J. Lin, S.Y.H. Liou, M.A. Bañares, M.O. Guerrero-Pérez, R.M. Martín Aranda, Enhanced cyclic CO2/N2 separation performance stability on chemically modified N-doped ordered mesoporous carbon, Catal. Today 356 (2020) 88−94, https://doi.org/10.1016/j.cattod.2019.08.004.

[31] A.Z. Peng, S.C. Qi, X. Liu, D.M. Xue, S.S. Peng, G.X. Yu, X.Q. Liu, L.B. Sun, Fabrication of N-doped porous carbons for enhanced CO2 capture: rational design of an ammoniated polymer precursor, Chem. Eng. J. 369 (2019) 170−179, https://doi.org/10.1016/j.cej.2019.03.038.

[32] F. Kleitz, S.H. Choi, R. Ryoo, Cubic Ia3d large mesoporous silica: synthesis and replication to platinum nanowires, carbon nanorods and carbon nanotubes, Chem. Commun. 3 (2003) 2136−2137, https://doi.org/10.1039/b306504a.

[33] S.H. Joo, S. Jun, R. Ryoo, Synthesis of ordered mesoporous carbon molecular sieves CMK-1, Microporous Mesoporous Mater. 44−45 (2001) 153−158, https://doi.org/10.1016/S1387-1811(01)00179-2.

[34] S. Jun, Sang Hoon Joo, R. Ryoo, M. Kruk, M. Jaroniec, Z. Liu, T. Ohsuna, O. Terasaki, Synthesis of new, nanoporous carbon with hexagonally ordered mesostructure [5], J. Am. Chem. Soc. 122 (2000) 10712−10713, https://doi.org/10.1021/ja002261e.

[35] L.L. Perreault, S. Giret, M. Gagnon, J. Florek, D. Larivière, F. Kleitz, Functionalization of mesoporous carbon materials for selective separation of lanthanides under acidic conditions, ACS Appl. Mater. Interfaces 9 (2017) 12003−12012, https://doi.org/10.1021/acsami.6b16650.

[36] K.A. Cychosz, M. Thommes, Progress in the physisorption characterization of nanoporous gas storage materials, Engineering 4 (2018) 559−566, https://doi.org/10.1016/j.eng.2018.06.001.

[37] J. Pires, V.K. Saini, M.L. Pinto, Studies on selective adsorption of biogas components on pillared clays: approach for biogas improvement, Environ. Sci. Technol. 42 (2008) 8727−8732, https://doi.org/10.1021/es8014666.

[38] L.A. Solovyov, V.I. Zaikovskii, A.N. Shmakov, O.V. Belousov, R. Ryoo, Framework characterization of mesostructured carbon CMK-1 by X-ray powder diffraction and electron microscopy, J. Phys. Chem. B 106 (2002) 12198−12202, https://doi.org/10.1021/jp0257653.

[39] T.W. Kim, F. Kleitz, B. Paul, R. Ryoo, MCM-48-like large mesoporous silicas with tailored pore structure: facile synthesis domain in a ternary triblock copolymer-butanol-water system, J. Am. Chem. Soc. 127 (2005) 7601−7610, https://doi.org/10.1021/ja042601m.

[40] M. Kaneda, T. Tsubakiyama, A. Carlsson, Y. Sakamoto, T. Ohsuna, O. Terasaki, S.H. Joo, R. Ryoo, Structural study of mesoporous MCM-48 and carbon networks synthesized in the spaces of MCM-48 by electron crystallography, J. Phys. Chem. B 106 (2002) 1256−1266, https://doi.org/10.1021/jp0131875.

[41] M. Kruk, M. Jaroniec, R. Ryoo, S.H. Joo, Characterization of ordered mesoporous carbons synthesized using MCM-48 silicas as templates, J. Phys. Chem. B 104 (2000) 7960−7968, https://doi.org/10.1021/jp000861u.

[42] Y.J. Sa, K. Kwon, J.Y. Cheon, F. Kleitz, S.H. Joo, Ordered mesoporous Co3O4 spinels as stable, bifunctional, noble metal-free oxygen electrocatalysts, J. Mater. Chem. A. 1 (2013) 9992−10001, https://doi.org/10.1039/c3ta11917c.

[43] M. Thommes, K. Kaneko, A.V. Neimark, J.P. Olivier, F. Rodriguez-Reinoso, J. Rouquerol, K.S.W. Sing, Physisorption of gases, with special reference to the evaluation of surface area and pore size distribution (IUPAC Technical Report), Pure Appl. Chem. 87 (2015) 1051−1069, https://doi.org/10.1515/pac-2014-1117.

[44] F. Jiao, A.H. Hill, A. Harrison, A. Berko, A.V. Chadwick, P.G. Bruce, Synthesis of ordered mesoporous NiO with crystalline walls and a bimodal pore size distribution, J. Am. Chem. Soc. 130 (2008) 5262−5266, https://doi.org/10.1021/ja710849r.

[45] T. Grewe, X. Deng, H. Tüysüz, A study on the growth of Cr2O3 in ordered mesoporous silica and its replication, Chem. Eur J. 20 (2014) 7692−7697, https://doi.org/10.1002/chem.201402301.

[46] M. Thommes, K.A. Cychosz, Physical adsorption characterization of nanoporous materials: progress and challenges, Adsorption 20 (2014) 233−250, https://doi.org/10.1007/s10450-014-9606-z.

[47] R. Konnola, T.S. Anirudhan, Efficient carbon dioxide capture by nitrogen and sulfur dual-doped mesoporous carbon spheres from polybenzoxazines synthesized by a simple strategy, J. Environ. Chem. Eng. 8 (2020) 103614, https://doi.org/10.1016/j.jece.2019.103614.

[48] Y. Meng, D. Gu, F. Zhang, Y. Shi, L. Cheng, D. Feng, Z. Wu, Z. Chen, Y. Wan, A. Stein, D. Zhao, A family of highly ordered mesoporous polymer resin and carbon structures from organic-organic self-assembly, Chem. Mater. 18 (2006) 4447−4464, https://doi.org/10.1021/cm060921u.

[49] M. Ayiania, M. Smith, A.J.R. Hensley, L. Scudiero, J.S. McEwen, M. Garcia-Perez, Deconvoluting the XPS spectra for nitrogen-doped chars: an analysis from first principles, Carbon N. Y. 162 (2020) 528−544, https://doi.org/10.1016/j.carbon.2020.02.065.

[50] Y. Wang, X. Hu, J. Hao, R. Ma, Q. Guo, H. Gao, H. Bai, Nitrogen and oxygen codoped porous carbon with superior CO2 adsorption performance: a combined experimental and DFT calculation study, Ind. Eng. Chem. Res. 58 (2019) 13390−13400, https://doi.org/10.1021/acs.iecr.9b01454.

[51] K. Stańczyk, R. Dziembaj, Z. Piwowarska, S. Witkowski, Transformation of nitrogen structures in carbonization of model compounds determined by XPS, Carbon N. Y. 33 (1995) 1383−1392, https://doi.org/10.1016/0008-6223(95)00084-Q.

[52] M. Gehring, H. Tempel, A. Merlen, R. Schierholz, R.A. Eichel, H. Kungl, Carbonisation temperature dependence of electrochemical activity of nitrogen-doped carbon fibres from electrospinning as air-cathodes for aqueous-alkaline metal-air batteries, RSC Adv. 9 (2019) 27231−27241, https://doi.org/10.1039/c9ra03805a.

[53] A. Gonciaruk, M.R. Hall, M.W. Fay, C.D.J. Parmenter, C.H. Vane, A.N. Khlobystov, N. Ripepi, Kerogen nanoscale structure and CO2 adsorption in shale micropores, Sci. Rep. 11 (2021) 1−13, https://doi.org/10.1038/s41598-021-83179-z.

[54] M.V. Zakharova, N. Masoumifard, Y. Hu, J. Han, F. Kleitz, F.G. Fontaine, Designed synthesis of mesoporous solid-supported Lewis acid-base pairs and their CO2 adsorption behaviors, ACS Appl. Mater. Interfaces 10 (2018) 13199−13210, https://doi.org/10.1021/acsami.8b00640.

[55] A. Samanta, A. Zhao, G.K.H. Shimizu, P. Sarkar, R. Gupta, Post-combustion CO 2 capture using solid sorbents: a review, Ind. Eng. Chem. Res. 51 (2012) 1438−1463, https://doi.org/10.1021/ie200686q.

[56] M. Oschatz, M. Antonietti, A search for selectivity to enable CO2 capture with porous adsorbents, Energy Environ. Sci. 11 (2018) 57−70, https://doi.org/10.1039/c7ee02110k.

[57] Y. Zhao, X. Liu, Y. Han, Microporous carbonaceous adsorbents for CO2 separation via selective adsorption, RSC Adv. 5 (2015) 30310−30330, https://doi.org/10.1039/c5ra00569h.

[58] P. Pornaroontham, G. Panomsuwan, S. Chae, N. Saito, N. Thouchprasitchai, Y. Phongboonchoo, S. Pongstabodee, Nitriding an oxygen-doped nanocarbonaceous sorbent synthesized via solution plasma process for improving CO2 adsorption capacity, Nanomaterials 9 (2019), https://doi.org/10.3390/nano9121776.

[59] Á. Sánchez-Sánchez, F. Suárez-García, A. Martínez-Alonso, J.M.D. Tascón, Influence of porous texture and surface chemistry on the CO2 adsorption capacity of porous carbons: acidic and basic site interactions, ACS Appl. Mater. Interfaces 6 (2014) 21237−21247, https://doi.org/10.1021/am506176e.

[60] H. Yuan, J. Chen, D. Li, H. Chen, Y. Chen, 5 Ultramicropore-rich renewable porous carbon from biomass tar with excellent adsorption capacity and selectivity for CO2 capture, Chem. Eng. J. 373 (2019) 171−178, https://doi.org/10.1016/j.cej.2019.04.206.

[61] G. Lim, K.B. Lee, H.C. Ham, Effect of N-containing functional groups on CO2 adsorption of carbonaceous materials: a density functional theory approach, J. Phys. Chem. C 120 (2016) 8087−8095, https://doi.org/10.1021/acs.jpcc.5b12090.

[62] F. Sun, X. Liu, J. Gao, X. Pi, L. Wang, Z. Qu, Y. Qin, Highlighting the role of nitrogen doping in enhancing CO2 uptake onto carbon surfaces: a combined experimental and computational analysis, J. Mater. Chem. A. 4 (2016) 18248−18252, https://doi.org/10.1039/c6ta08262a.

[63] D. Wu, J. Liu, Y. Yang, Y. Zheng, Nitrogen/oxygen Co-doped porous carbon derived from biomass for low-pressure CO2Capture, Ind. Eng. Chem. Res. 59 (2020) 14055−14063, https://doi.org/10.1021/acs.iecr.0c00006.

[64] D. Wu, Y. Yang, J. Liu, Y. Zheng, Plasma-Modified N/O-doped porous carbon for CO2Capture: an experimental and theoretical study, Energy Fuel 34 (2020) 6077−6084, https://doi.org/10.1021/acs.energyfuels.0c00415.

[65] S.D. Kenarsari, D. Yang, G. Jiang, S. Zhang, J. Wang, A.G. Russell, Q. Wei, M. Fan, Review of recent advances in carbon dioxide separation and capture, RSC Adv. 3 (2013) 22739−22773, https://doi.org/10.1039/c3ra43965h.

[66] P. Serra-Crespo, E.V. Ramos-Fernandez, J. Gascon, F. Kapteijn, Synthesis and characterization of an amino functionalized MIL-101(Al): separation and catalytic properties, Chem. Mater. 23 (2011) 2565−2572, https://doi.org/10.1021/cm103644b.

[67] Z. Zhang, N. Sun, W. Wei, Facile and controllable synthesis of ordered mesoporous carbons with tunable single-crystal morphology for CO2 capture, Carbon N. Y. 161 (2020) 629−638, https://doi.org/10.1016/j.carbon.2020.02.009.

[68] M. Vorokhta, J. Morávková, M. Dopita, A. Zhigunov, M. Šlouf, R. Pilař, P. Sazama, Effect of micropores on CO2 capture in ordered mesoporous CMK-3 carbon at atmospheric pressure, Adsorption (2021), https://doi.org/10.1007/s10450-021-00322-y.

[69] X. Wan, Y. Li, H. Xiao, Y. Pan, J. Liu, Hydrothermal synthesis of nitrogen-doped ordered mesoporous carbon: via lysine-assisted self-assembly for efficient CO2 capture, RSC Adv. 10 (2020) 2932−2941, https://doi.org/10.1039/c9ra09983b.

[70] W. Kong, J. Liu, Ordered mesoporous carbon with enhanced porosity to support organic amines: efficient nanocomposites for the selective capture of CO2, New J. Chem. 43 (2019) 6040−6047, https://doi.org/10.1039/c9nj00617f.

[71] X. Liu, Y. Zhou, C.L. Wang, Y. Liu, D.J. Tao, Solvent-free self-assembly synthesis of N-doped ordered mesoporous carbons as effective and bifunctional materials for CO2 capture and oxygen reduction reaction, Chem. Eng. J. 427 (2022) 130878, https://doi.org/10.1016/j.cej.2021.130878.